Interparticle bonding and interfacial nanocrystallization mechanisms in cold sprayed metallic glass

Ningsong Fan [a], Chunjie Huang [b], Pengfei Yu [a], Wen Chen [c], Rocco Lupoi [a], Lin Liu [d], Shuo Yin [a]

[a] Department of Mechanical, Manufacturing & Biomedical Engineering, Parsons Building, Trinity College Dublin, The University of Dublin, Dublin 2, Ireland
[b] Institute of Materials Technology, Helmut-Schmidt-University/University of the Federal Armed Forces Hamburg, 22043 Hamburg, Germany
[c] Department of Mechanical and Industrial Engineering, University of Massachusetts, Amherst, MA 01003, United States
[d] State Key Laboratory of Materials Processing and Die & Mould Technology, School of Materials Science and Engineering, Huazhong University of Science and Technology, Wuhan 430074, China

Abstract: In this work, amorphous Zr-based bulk metallic glass deposit was manufactured by cold spray. The bonding mechanism of metallic glass particles was systematically investigated through studying the deformation behavior of individual particles after deposition or rebound. We revealed two collective particle bonding mechanisms that contributed to the formation of metallic glass deposit, i.e., high-velocity impact induced localized metallurgical bonding at the fringe of interface, and high gas-temperature induced partial melting of particles and resultant annular metallurgical bonding band. Moreover, the dynamic evolution mechanism of amorphous phase into nanocrystal structures at severely deformed interfacial regions during cold spray was carefully investigated. For the first time, we observed different amorphous/nanocrystal structures in cold sprayed metallic glass particles, which can represent different evolution stages in nanocrystallization process. Based on the observation, it is inferred that the nanocrystallization process can be divided into following three stages: composition segregation, the formation of ordered 1D and 2D transition structures, and 3D nanocrystals. The current study provides new insights into bonding mechanisms and the mechanistic nanocrystallization origins in cold sprayed metallic glass.

1 Introduction

Metallic glasses, also known as amorphous alloys, are a class of advanced multi-component alloy with unique long-range disordered but short-range ordered structures. The unique amorphous structure results in the absence of crystalline defects (e.g., grain boundaries, dislocations, and stacking faults), leading to the high performance of metallic glasses [1,2]. Metallic glasses are typically fabricated through rapid solidification of molten liquids to bypass crystallization. However, it has been particularly challenging to produce bulk metallic glasses (BMGs) by using traditional manufacturing method. In recent decades, promising additive manufacturing techniques have been developed for the production of BMGs, such as laser cladding [3], laser solid forming [4], selective laser melting [5] and some thermal spray processes [6–8]. These additive manufacturing routes allow the fabrication of large-scale components and have attracted attentions from both scientific and industrial communities. Nevertheless, the complicated thermal history associated with these fusion-based processes usually results in detrimental metallurgical defects (e.g., phase transformation, oxidation, and severe crystallization) that deteriorate the mechanical properties of BMGs.

Cold spray is an emerging material deposition and solid-state additive manufacturing technology, which provides an alternative to produce BMGs. In this process, micro-sized metal feedstock powder is accelerated to supersonic in a de-Laval nozzle by compressed nitrogen or helium at elevated temperatures well below their melting points, and projected onto a substrate.The kinetic energy causes severe plastic deformation of powder upon impact and the particles can bond through metallicgical bonding and mechanical interlocking, which allows the consolidation of powder to deposit layer-by-layer. The low processing temperature in cold spray helps to minimize thermal influences, and thereby retains a high extent of amorphous structure in BMG deposits. In cold spray, extensive plastic deformation of spraying material is expected to achieve dense deposit with good interparticle bonding. The plastic deformation behavior of metallic glasses highly depends on temperature and strain rate [9]. Metallic glasses experience inhomogeneous deformation at low temperatures and high strain rates, which can be characterized by severe localized plastic flow concentrated within thin shear bands. In contrast, homogeneous deformation of metallic glasses generally takes place at higher temperatures (typically in or near supercooled liquid region, which is defined as the temperature interval between glass transition temperature (T_g) and crystallization temperature (T_x)) or lower strain rates. Furthermore, it features a transition from Newtonian flow to non-Newtonian flow with increasing strain rate. In supercooled liquid region, metallic glasses generally exhibit distinct viscous flow and superplastic deformation characteristics. The excellent processability of metallic glasses in the supercooled liquid region allows net-shape forming. Therefore, metallic glass particles are usually preheated to supercooled liquid region in cold spray to achieve better particle bonding and higher deposition efficiency [10,11].

Researchers have studied the formation mechanism of cold sprayed BMG deposits through investigating the deformation behavior of individual particles after high-velocity impact. Yoon et al. [12] classified a deposited Ni-based metallic glass particle into three characteristic regions: “little (or no) deformation” at the north pole of a particle, “shear bands and fracture” at the periphery of a particle, and “melting and viscous flow” features at the bottom, which suggested the generation of strain and temperature gradients in deposited particles. The successful bonding of particles was considered to be related to the viscous flow and melting at impacting interface, driven by the adiabatic heating [12]. Further, another study pointed out that melting only occurred at the bottom periphery (the fringe of interface) rather than the entire region as evidenced by the pronounced vein patterns at the bottom of a detached Cu-based metallic glass particle [13]. Henao et al. [14] investigated the homogeneous deformation of individual Zr-based metallic glass particle with finite element method, which used the viscoplastic equations based on free-volume constitutive theory. Their study revealed that the non-Newtonian behavior (shear shinning) promoted the extensive viscoplastic deformation of metallic glass particles, and the homogeneous deformation, including both non-Newtonian and Newtonian flow, promoted the lateral viscous flow of metallic glass particles. The high temperature at impacting interface allowed the particle to bond with the substrate by metallurgical bonding. These two factors resulted in the formation of cold sprayed BMG deposits [14]. To sum up, the major contribution of the aforementioned studies is that they successfully revealed the important role of impact velocity and impact temperature in the deposition of cold sprayed metallic glass particles and concluded that melting and viscous flow were critical for the particle bonding of metallic glass. However, these studies did not clearly identify and demonstrate the exact bonding location at interparticle interface via experiment. Moreover, all the relevant studies attributed the particle bonding mechanism to the adiabatic-heating-induced melting and viscous flow. Nevertheless, in our experiments, we found another important mechanism that also contributed to the bonding of cold sprayed metallic glass particles, which has never been reported in previous studies. Therefore, the first motivation of this work is to introduce our new findings associated with the bonding mechanism of cold sprayed metallic glass particles.

Metallic glasses are thermodynamically metastable and tend to transform into their crystalline counterparts when supplied with sufficient energy to overcome the activation barriers associated with the nucleation and growth, e.g., through external stimuli such as mechanical deformation [15,16], thermal annealing [17], and electron irradiation [18]. For cold spray, nano-sized crystals were observed at the interface of a deposited Cu-based metallic glass particle, and the area of these nanocrystalline phases increased with the increased gas pressure [19]. On this basis, it is concluded that the nanocrystallization was associated with abnormally increased strain at highly deformed region, which was determined by the kinetic energy of particles upon impact. Although the study has attempted to interpret the crystallization behavior of metallic particles during cold spray, the role of temperature, strain and strain rate in the nanocrystallization event requires to be explored in great detail. Most importantly, the existing studies did not interpret how amorphous structure dynamically evolved into nanocrystals during cold spray deposition (i.e., crystallization mechanism). A good understanding of these two facts is rather critical to fully unlock the microstructure evolution of metallic glass particles during cold spray process, and this is the second motivation of this work.

2 Experimental methodology

2.1 Cold spray deposition process

Gas atomized $Zr_{55}Cu_{30}Ni_5Al_{10}$ (at%, hereafter referred to as Zr55) amorphous powder (< 80 μm) were used as feedstock for cold spray due to its good glass forming ability which allowed to produce large-scale metallic glass. **Fig. 1** shows the surface morphology of the as-atomized Zr55 amorphous powder characterized by scanning electron microscope (SEM, Carl Zeiss ULTRA Plus, Germany). The majority of the feedstock powder are highly spherical with smooth surfaces. The deposition of Zr55 was achieved by using an in-house cold spray system (Trinity College Dublin, Ireland) as mentioned in our precious work [20]. Compressed nitrogen was selected as propelling gas, and the gas pressure and the temperature were 3.0 MPa and 800 °C, respectively. The standoff distance from the exit of de-Laval Nozzle to the target surface was kept at 30 mm. Two experiments, namely full deposit and single splat deposit, were performed to explore the microstructural evolution and the formation mechanism of the cold sprayed Zr55 deposits. For the full deposit, thick Zr55 deposit was deposited onto Al substrate under a nozzle traversal speed of 50 mm/s and a powder feeding rate of 50 g/min. The nozzle moving trajectory followed a reciprocating zigzag strategy, and the space between two neighboring tracks was 3.0 mm. For the single splat deposit, Zr55 particles were deposited onto mirror-polished cold sprayed Zr55 deposit under a nozzle traversal speed of 150 mm/s and a lower powder feeding rate (10 g/min). The reason for using the as-sprayed Zr55 deposit as substrate is to simulate the particle-on-particle deposition process during the practical cold spray process.

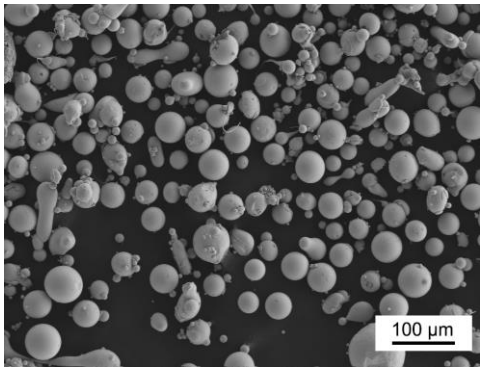

Figure 1. Surface morphology of as-atomized Zr55 metallic glass feedstock powder

2.2 Microstructure characterization

As preparatory work for microstructure analysis, the cross-sectional sample was prepared using standard metallographic procedures. The microstructure of the cold sprayed Zr55 deposit was characterized by SEM. The element compositions of the Zr55 deposit were examined by energy dispersive X-Ray spectroscopy (EDS, Oxford Instruments INCA, UK). The density of the deposit was estimated by optical microscopy (Leica DM LM, Germany) with image analysis method. The result was averaged from five different regions of the deposit to ensure the reliability of data. The phase structure of the Zr55 deposit was analyzed by X-ray diffraction (XRD, Bruker D8, Germany) equipped with Cu-Kα radiation from a range of 2θ values between 20° and 80° (40 kV, 40 mA) at a scanning rate of 1.2° min^{-1}. The micro- and nano-structure at the highly deformed region near the interparticle interfaces were characterized by transmission electron microscopy (TEM, FEI Tecnai G2 F20) in combination with selected area electron diffraction (SAED). The lamella for TEM characterization was extracted by focused ion beam (FIB, FEI Scios). The Fast Fourier transformation (FFT) patterns of the selected regions on TEM images were converted by commercial software (Digital Microscopy, Gatan). Furthermore, the surface and the cross-sectional morphology of individual Zr55 splats were characterized by SEM, and the cross-sections were prepared through FIB milling.

3 Results and discussion

3.1 Microstructure and phase composition

Fig. 2a shows the cross-sectional microstructure of the cold sprayed Zr55 deposit. The deposit is highly dense with few microstructural defects such as pores and cracks. The density of the deposit was measured to be 99.70 ± 0.13%. In cold spray, defect-free deposit normally suggests that particles experience extensive plastic deformation during deposition and interparticle bonding is promising. The EDS mapping results provided in **Fig. 2b** indicate that there is no chemical segregation or oxide inclusion in the deposit. This fact indicates the promise of cold spray for fabricating BMGs with high purity. **Fig. 2c** displays the XRD spectrum conducted on the cross-sectional Zr55 deposit. The XRD spectrum shows a broad diffraction peak maximum at around 2θ = 37° without any sharp diffraction peaks, indicating that the deposit retained an amorphous structure at the detection limit of XRD. This result stands contrast with the XRD spectra of BMGs made by other fusion-based additive manufacturing techniques that often exhibit sharp crystallization peaks [4,21]. Therefore, compared with other additive manufacturing techniques, the inherent characteristics of cold spray such as low temperature, short impacting period, and high cooling rates mitigate the challenge of severe crystallization during the deposition process. However, it is noteworthy that that the deposit may experience nanocrystallization, particularly at the highly deformed impacting interface as previous reported [19].

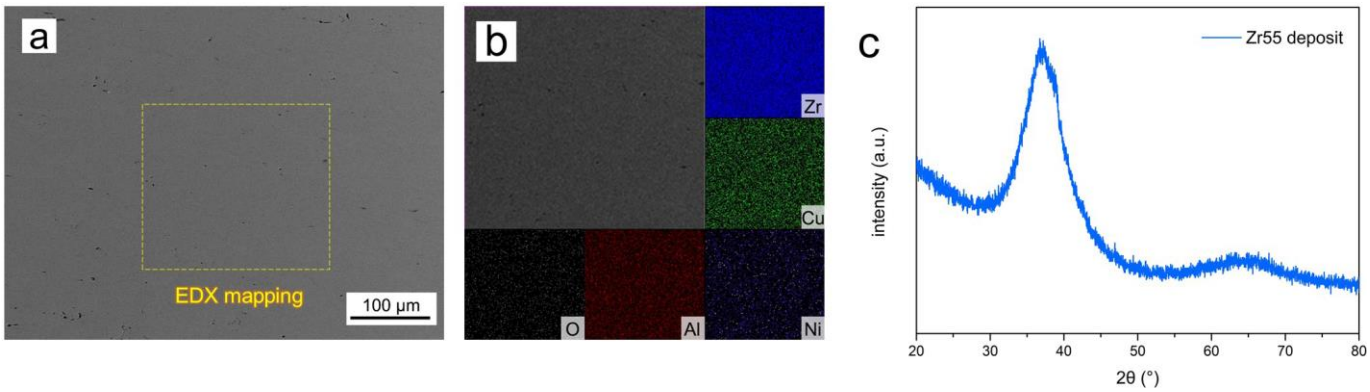

Figure 2. Characterization of the cold sprayed Zr55 deposit: (a) cross-sectional microstructure, (b) EDS map of elements distribution, (c) XRD spectrum.

3.2 Interparticle bonding mechanisms in cold sprayed Zr55 metallic glass

Fig. 3 shows the representative surface morphologies of individual Zr55 particles after impact, and craters created by rebound particles. **Fig. 3a** shows a deposited particle with high sphericity. It can be seen that shear bands and shear cracks were generated in the particle, which are the typical characteristics of localized flow (inhomogeneous deformation at high strain rates) of metallic glasses. When the particle impacted onto the substrate, the stress at the contact interface increased quickly. Once the stress reached a critical value, yielding occurred and permanent shape change was observed macroscopically through the initiation of shear bands. The shear bands initiated from the bottom of the particle and propagated rapidly towards the north pole with the stress waves travelling the particle. The dominant shear bands finally developed into cracks. In addition, thin squeezed material was found at the bottom periphery of the deposited particle, which is the evidence of viscous fluid or melting fluid induced by high temperature and shear strain. **Fig. 3b** shows a deposited particle with more significant localized flow features (i.e., increased number of shear bands and larger area of shear surface), which could be attributed to higher kinetic energy of the particle. The shear surface presents vein pattern and white ridge lines at sub-micron scale, indicating the localized softening by adiabatic heating during the rapid shear. Besides, there are some splashing melting (or viscous fluid) jets around the particle as pointed by yellow arrow, which suggests the extremely high temperature localized at the bottom of the particle. As shown in **Fig. 3c**, the particle experienced more severe localized plastic deformation and deformed to a propeller-like shape with further increased area of shear surface. In addition, the shear surface presents flat and smooth appearance, which is quite different from that in **Fig. 3b**. This could resulted from the extreme adiabatic temperature during shear banding at higher strain rates, and the temperature within the shear bands may reach the melting point T_m (1028K [22]). It is reported that the temperature rise associated with shear banding in metallic glass can reach up to a few thousand kelvin over a few nanoseconds [23]. Such high temperature and high strain rate led to sharply decreased viscosity and thus the smooth shear surface.

Fig. 3d shows a deposited particle with its right part fractured and ejected after impact due to severe shear localization, which provides an opportunity to observe what happened at the bottom of the particle. A large volume of viscous fluid or melting fluid can be observed at the bottom region of the particle. This is because of the adiabatic heating induced by highly localized plastic deformation upon impact. Accordingly, there is a reasonable prospect that localized viscous fluid or melting fluid induced by high temperature occurred surrounding the peripheral of the south pole of the deposited particle, resulting in particle adhesion to substrate. The viscous fluid or melting fluid is the strong evidence of homogeneous deformation of metallic glass particle.

Figs. 3e-f show craters on the substrate surface created by rebound Zr55 particles. As shown in **Fig. 3e**, the central region of the crater is rather clean with nearly no evidences of metallurgical bonding between the particle and substrate. However, a ring of dimple-like structures (vein pattern as marked by yellow arrows) can be observed at the surrounding area of the crater together with some “melting fluid jets” (or viscous fluid jets). These dimple-like features and viscous jets are the result of the high temperature at the impacting interface. The increased temperature led to the sharp decrease of viscosity, which promoted viscous flow at the bottom periphery of the particle. Actually, the most interesting finding from **Figs. 3e-f** is that these dimple-like materials remained bonded with the substrate after particle rebounding. The detachment occurred in the particle rather than from the particle-substrate interface. This fact indicates that Zr55 particle can bond with the substrate upon impact in the first place. However, the viscous force of the liquefied interface failed to surpass the particle rebounding force, thus the particle rebounded from the substrate after adiabatic impacting. Therefore, it can be inferred that successful bonding requires adequate viscous force generated by dimple-like materials between substrate and Zr55 particle.

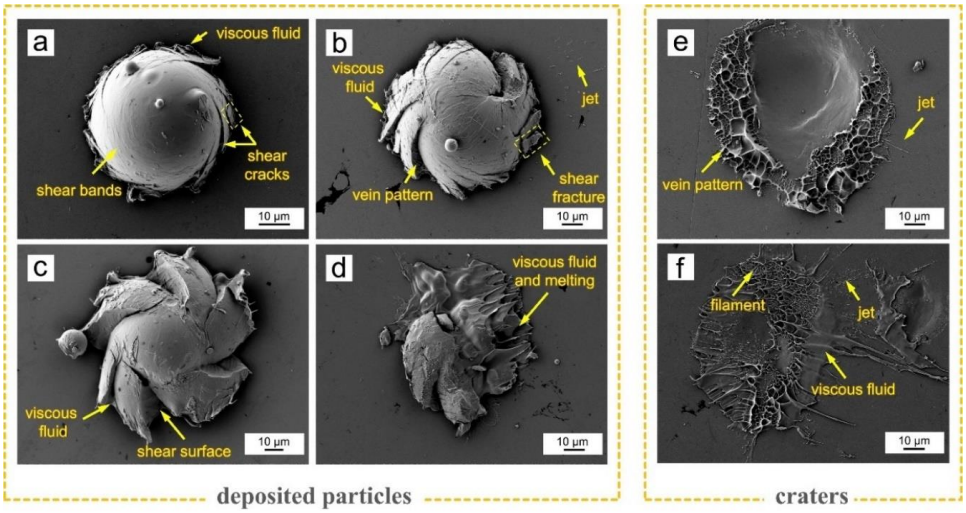

Figure 3. Top view of the representative surface morphologies of (a)-(d) individual Zr55 deposited particles and (e)-(f) craters created by rebound Zr55 particles.

In order to observe what had happened at the interface exactly and how the metallic glass particles bonded with previous deposited layer, a deposited Zr55 particle was dug from the top with FIB to display the entire particle-substrate interface. **Fig. 4** exhibits the surface morphology of a particle after impact and corresponding cross-sectional morphology including particle-substrate interface. As shown in **Fig. 4a**, the deposited particle is characterized by severe shear localization which is the feature of inhomogeneous deformation, representing the common deposition morphology for Zr55 particles. **Figs. 4b-c** show the cross-sectional morphology of the deposited particle. There is a nanoscale gap between the deposited particle and substrate except at the fringe of the interface at which the particle bonded with the substrate. The formation of nanoscale gap can be attributed to the back spring elastic forces. The bonding only occurred at the fringe of particle-substrate interface, which is consistent with what we see in the crater (see **Fig. 3e)**. This is the first time that the exact bonding location of metallic glass particles was observed experimentally.

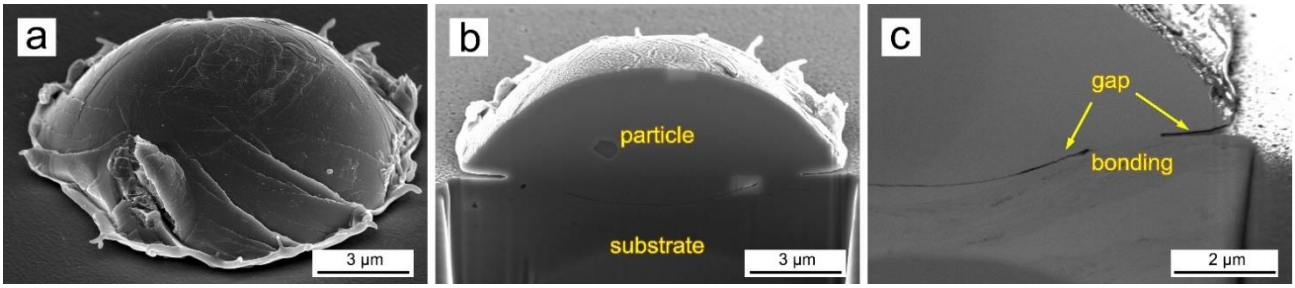

Figure 4. FIB process of individual Zr55 deposited particle: (a) surface morphology, (b) cross-sectional morphology revealing particle-substrate interface, (c) close view of metallurgical bonding at the interface.

The outer layers of all the deposited particles in **Fig. 3** exhibit the same surface status as feedstock without any trace of viscous fluid or melting fluid, which implies that the surface temperature of these particles was relatively low before impacting. However, the deposited particle, as shown in **Fig. 5a**, presents an exceptional status where the outer layer of the particle was melted. Compared with the particles in **Fig. 4**, there are no visible shear bands, cracks or fractures, indicating the particle mainly experienced homogeneous deformation. This is probably because the outer layer of the particle melted inside the nozzle. The gas temperature used for single splat deposition (800 °C) was higher than the T_m (~755 °C [22]), but lower than the liquidus temperature T_l (~ 890 °C [24]) of Zr55 metallic glass. Although the gas temperature decreased in the nozzle, the particles still had chance to be partially melted in the prechamber or convergent section of the nozzle, particularly for large-sized particles, which had longer residence. Similar to preheated particles, higher temperature favors particle global deformation and bonding. The bonding mechanism of such particle is associated with the melted outer layer of the particle.

Figs. 5c-d show the cross-sectional morphology of the deposited particle. Discontinuous gap between particle and substrate was found at the highly deformed region. However, the close view at the side of the interface shows an annular metallurgical bonding band with a thickness of ~1 μm, which is quite different from the metallurgical bonding area in **Fig. 4c**. When the particle with melted outer layer impacted onto the substrate at high velocity, the viscous fluid was forced to flow to the periphery. The viscous fluid at the side of interface adhered with the substrate through metallurgical bonding. It is noteworthy that the number of particles bonded in this mode was quite limited according to our observation of the microscopic graphs. The partial melting of the particles in the nozzle is affected by many factors, such as particle size and in-flight trajectory. In general, large-sized particles are likely to be partially melted due to their longer residence. Moreover, particles travelling through the centre of the nozzle experience higher gas temperature, compared with those particles travelling near the inner wall of nozzle. In brief, some particles were probably subjected to partial melting inside the nozzle and adhered with the substrate through annular metallurgical bonding band after impact, which is different from the impact induced localized metallurgical bonding.

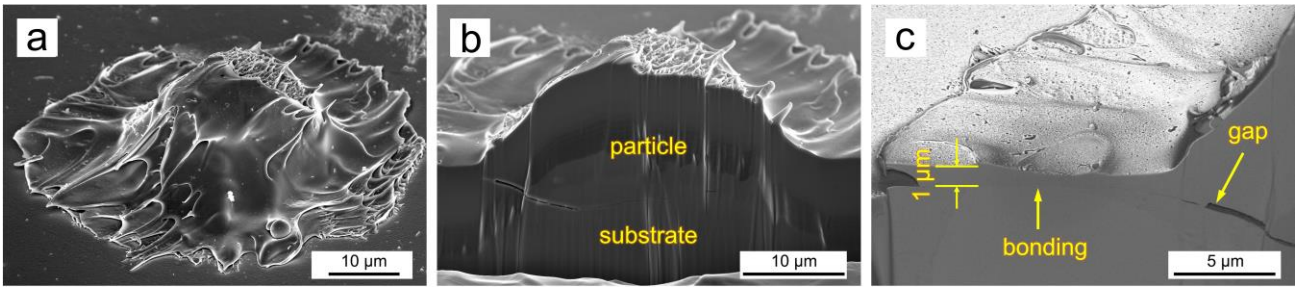

Figure 5. FIB process of individual Zr55 deposited particle with melted outer layer: (a) surface morphology, (b) cross-sectional morphology revealing particle-substrate interface, (c) close view of metallurgical bonding at interface.

Based on the results and discussion presented above, it is sensible to conclude that the bonding of the cold sprayed Zr55 particles can be achieved through two different mechanisms. For most of the deposited particles, the bonding was realized by the high-velocity impact induced localized metallurgical bonding at the fringe of interface. The rising temperature at impacting interface led to the sharp decrease of viscosity, and promoted lateral homogeneous deformation at the bottom of metallic glass particles. However, the impact velocity of particles cannot be too much high to prevent particle rebounding from the substrate. Apart from this, an unusual particle bonding mechanism that has never been reported was also found to contribute to the deposition of metallic glass particles. The high gas temperature (above T_m of Zr55) in the nozzle can induce partial melting of particles. Upon impact, the melted outer layer was forced to flow to periphery and adhered with the substrate through an annular metallurgical bonding band. The partial melting of the particle in the nozzle is related to the particle size and the in-flight trajectory. Specifically, a particle with larger size or travelling through the center of nozzle is more likely to experience partial melting due to longer residence or higher gas temperature. Both two particle bonding modes contribute to the formation of the cold sprayed Zr55 deposit.

3.3 Interficial nanocrystallization mechanisms in cold sprayed Zr55 metallic glass

Fig. 6a shows the interface between two metallic glass particles in the cold sprayed Zr55 deposit observed by SEM. The lamella containing interparticle interface, as shown in **Fig. 6b**, was then lifted out by FIB. The nanostructure of two regions S1 (away from the interparticle interface) and S2 (near the interparticle interface) was investigated by TEM. **Fig. 6c** shows the bright field TEM image and corresponding SAED pattern of a region in S1. The diffusion halo in SAED pattern indicates that a glass structure in amorphous phase was well-retained at the region away from the interparticle interface. However, a heterogeneous nanostructure with nano-scale dark polygon areas randomly dispersed in the amorphous matrix was observed at the extremely localized near-interface region (S2), as shown in **Fig. 6d**. The corresponding SAED pattern displays diffuse halo rings with few irregular bright specks, suggesting the coexistence of amorphous and nanocrystal structures. These nanocrystals with dark polygonal structures were believed to form during the particle deposition.

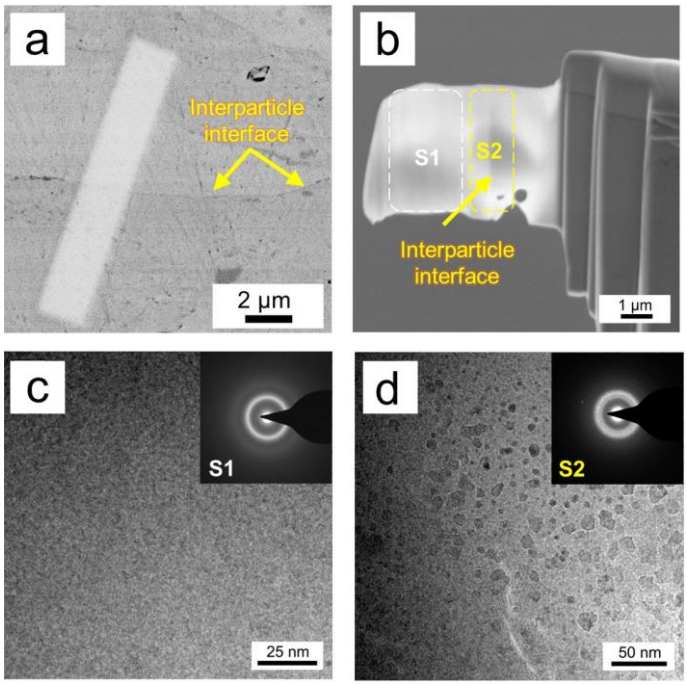

Figure 6. Characterization of the nanostructure at interparticle interface: (a) SEM image exhibiting interparticle boundary between two particles, (b) SEM image of the lamella lifted out by FIB, (c)-(d) TEM micrograph with SAED pattern inset (c) away from the interparticle interface and (d) near the interparticle interface, respectively.

In cold spray process, adiabatic heating at impacting interface is unavoidable during the high-strain-rate deformation of particles, which leads to considerable temperature rise and material softening. The high temperature can reduce the energy barrier of atomic diffusion, and the formation of nanocrystals through the atomic diffusion mechanism of nucleation and growth in amorphous matrix is possible. In this work, the high temperature can be inferred from the melting jets surrounding the particle (see **Fig. 3**). However, it is notable that there is no driving force for nanocrystallization if the temperature is above the T_m. Moreover, the cooling rate in cold spray process can reach as high as 10^9~10^{10} $K \cdot s^{-1}$ at the highly deformed interfacial regions [25], which is significantly higher than that of gas atomized droplets (10^4~10^6 $K \cdot s^{-1}$ [26,27]). The gas atomized metallic glass powder can retain amorphous structure, so the cooling rate in cold spray is high enough to bypass nanocrystallization. In other words,

the effect of adiabatic heating on the formation of nanocrystals at interparticle interface is considered to be very limited.

In general, the atomic mobility in metallic glasses is frozen when it is cooled by glass transition [28]. However, the plastic deformation is able to assist atomic transportation and evolution toward equilibrium, and thereby inducing ordering of localized structure. In fact, the nanocrystallization of metallic glasses has been observed in various plastic deformation processes at room or cryogenic temperature, such as rolling [15], nanoindentation [29], high-pressure torsion [30], and ball milling [31], particularly in the region of deformed specimen under compressive stress. This indicates that the nanocrystals form in these low-temperature plastic deformation processes is due to the strain, rather than the deformation induced temperature rise.

Nucleation is a key step in the crystallization process. Crystals can be produced only when the size of nucleation exceeds a critical size. According to classical nucleation theory, the nucleation rate ($\dot{N}$) can be described as $\dot{N} = N\,exp(-\frac{\Delta G^*}{kT})\,exp(-\frac{\Delta E}{kT})$ [32], where N is a constant at a fixed temperature, ΔG^* is the energy barrier for nucleation required to form a critical sized nucleus, ΔE is the energy barrier for diffusion required to transport an atom from an amorphous matrix to an embryonic nuclei, k is the Boltzmann's constant. Therefore, the nucleation rate ($\dot{N}$) will increase if the energy barrier for nucleation (ΔG^*) and atomic diffusion (ΔE) are reduced.

The pressure (P) modified energy barrier to form a spherical crystal nucleus with a critical size (ΔG^*) can be expressed as $\Delta G^*(T,P) = \frac{16\pi\gamma^3}{3}(\frac{V_m^c}{\Delta G_m + E + P\Delta V_m})^2$ [32], where V_m^c is the molar volume of the crystalline phase, ΔG_m is the molar free energy difference between the amorphous and crystalline phases, E is the elastic energy induced by the volume change during the phase transformation in the solid state, γ is the interfacial free energy between the amorphous and crystalline phases, and ΔV is the volume change to form this crystalline nucleus from amorphous state.

During the phase transformation from amorphous to crystalline, the values of ΔG_m and ΔV_m ($\Delta V_m = V_m^c - V_m^a$) are negative and E is rather small [33]. Therefore, the free energy required to produce a critical nucleus size (ΔG^*) decreases with the increasing of pressure. In cold spray, the high pressure at the impacting interface leads to the decreased ΔG^*. Moreover, crystalline phase possesses smaller volume than that of amorphous, and the crystalline nuclei inlaid in the amorphous matrix are under internal tension. Hence, the applied compressive stress can relieve the tensile stress in the crystalline nuclei and thereby stabilize the crystalline nuclei [34].

Based on free volume theory, the strain during the plastic deformation of metallic glass could generate free volume and promote atomic transportation. Furthermore, the increase rate of free volume and saturated free-volume content increase with strain rate. Higher strain rate leads to higher increase rate of free volume and resultant more free volume generation than lower strain rate. Although the creation of free volume comes along with the annihilation of free volume, the creation rate of free volume at high strain rate exceeds the annihilation rate. Therefore, high strain and high-strain rate deformation could generate more free volumes. The increase of free volume leads to atomic dilatation and thereby reduction in the barrier for mobility of atoms in BMGs [35]. In cold spray, the high strain and high strain rate at impacting interface contribute to the rapid generation of free volume and the rapid transportation of atoms. From the perspective of kinetics, the enhanced atomic transportation can be understood as the decrease of energy barrier for atomic diffusion (ΔE). The decreased ΔG^* and ΔE work together to increase the nucleation rate, which promotes the precipitation of nanocrystals from amorphous matrix. Therefore, the effect of mechanical factors on the nanocrystallization in cold sprayed metallic glass may be decisive.

In order to investigate how amorphous structure dynamically evolved into nanocrystals during cold spray, high resolution transmission electron microscopy (HRTEM) and corresponding FFT patterns of localized dark regions were achieved as shown in **Fig. 7**. As a benchmark, the FFT pattern of the amorphous matrix (region I) is provided in the figure as well. Before starting discussion, it is worth pointing out that in this work we for the first time observed different amorphous/nanocrystal structures in cold sprayed metallic glass particles that we believed representing different evolution stages in nanocrystallization process, and this helps us to fully reveal the nanocrystallization mechanism of metallic glass particles during cold spray. In **Fig. 7a**, the contrast of region II is darker than that of amorphous matrix, which may indicate that the atomic arrangement here is special. However, the HRTEM image reveals a disordered atomic structure and its corresponding FFT pattern displays a diffuse halo, which is nearly the same as that of amorphous matrix (region I). This fact suggests that region II is still in amorphous state. The difference in contrast is likely due to the composition segregation in region II [36]. Such segregation is believed to be induced by high mechanical stress and adiabatic temperature rise generated during the high-velocity impact of particles, resulting in the formation of a large amount of free volumes and promoting atomic diffusion to accelerate the composition segregation [15,37]. The occurrence of composition segregation is closely related to the interatomic interactions in the alloy. A large difference in the heat of mixing, or a positive heat of mixing between two components can result in phase separation [38]. In Zr-Cu-Ni-Al alloy system, the Cu and Ni

atomic pairs show a positive heat of mixing (ΔH_{Cu-Ni} = 4 kJ/mol). The heats of mixing of Zr-Ni (ΔH_{Zr-Ni} = -49 kJ/mol) and Zr-Al (ΔH_{Zr-Al} = -44 kJ/mol) are more negative than that of other atomic pairs (ΔH_{Zr-Cu} = -23 kJ/mol, ΔH_{Ni-Al} = -22 kJ/mol and ΔH_{Cu-Al} = -1 kJ/mol, respectively) [39]. The strong attractive interaction of Cu-Ni, Zr-Ni and Zr-Al helps the occurrence of segregation in the amorphous matrix.

The atoms in region III show a disordered arrangement which is similar with region I. However, localized ordered atomic lines (or columns) were found in certain directions, as pointed by the yellow arrows. The clusters in the yellow box are regarded as the feature of imperfect ordered packing [40]. The corresponding FFT diffraction pattern displays a diffuse halo without any bright spots, indicating the entire atomic configuration in this region remains disordered. However, some blurred spots are able to be distinguished. Furthermore, the connection of any two blurred spots, which are symmetry of the central spot, is perpendicular to the corresponding atomic arrangement direction as pointed in region III. This indicates some atoms started to adjust their position towards an ordered packing. It is more interesting that the ordering process concurrently occurred along multiple directions.

In region IV, the formation of lattice fringes can be clearly observed. The atoms formed highly ordered atomic lines along an exclusive periodic direction through further adjusting their positions. The corresponding FFT diffraction pattern of this atomic configuration shows a diffuse halo together with clearly visible bright specks, indicating the coexistence of amorphous and ordering structure in the current region. In other words, nanocrystallization in this area was incomplete. Moreover, only two bright spots were observed in the FFT pattern, which indicates it has 1D periodic arrangement [41]. Based on the FFT pattern, the 1D periodic arrangement has a plane space of about 0.244 nm, which is the typical (103) plane space of Zr_2Cu. It is worthy to note that the maximum ramp peak of the deposit is located in (103) plane of Zr_2Cu as well. Consequently, it can be inferred that the 1D periodic nanocrystal structure is Zr_2Cu. Furthermore, (103) plane is a relatively low plan index for Zr_2Cu lattice, and the packing of atoms on this plane is denser than that of a plane with higher index. In other words, it is easy for atoms to migrate to a stable site. Therefore, a cluster of single direction atomic columns (1D periodicity) was firstly formed along the low index or close packed direction. Such quasi-ordered structure with 1D periodicity has also been reported in the nanocrystallization of other metallic glasses or even proteins, which was regarded as a primary step to reach a localized equilibrium state [41,42]. Compared with the atoms in region IV, the atoms in region V also exhibit the feature of 1D periodicity. However, localized ordered atomic lines were also formed in other directions. The corresponding FFT diffraction pattern also supports what we observed. Aside from two bright specks indicating the 1D periodicity, other spots with lower brightness were also found. The connection of any two blurred spots, which are symmetry of the central spot, is perpendicular to the corresponding localized ordered direction as pointed in region V. It can be inferred that the atoms continued to adjust their positions towards a higher-ordered atomic configuration (i.e., 2D or 3D periodicity).

For region VI, as shown in **Fig. 7b**, almost all the atoms exist in a highly ordered arrangement with 3D periodicity, demonstrating a higher level of nanocrystallization. The nanocrystal structure could be $AlZr_3$, $AlCu_2Zr$ or $AlNi_2Zr$ on the [011] zone axis by calibration. The formation of above intermetallic is likely to be associated with a large difference in the heat of mixing, or a positive heat of mixing of corresponding elements in Zr55 alloy system. Although the arrangement of atoms in region VI was more orderly, crystal defects (e.g., dislocation or vacancy) were still exist in nanocrystal structure.

Based on the results and discussion above, the nanocrystallization mechanism of the cold sprayed Zr-based BMG deposit can be summarized as below. When the metallic glass particles impacted onto substrate at high velocity, the localized interfacial regions underwent severe plastic deformation at extremely high strain rates. The composition segregation induced by mechanical and thermal activation was dramatically promoted due to the increased number of free volumes and enhanced atomic diffusion, as shown in region II which presents dark and light difference. The segregation acted as a precursor for further nanocrystallization process. The atoms started to adjust their positions to form localized ordered atomic lines towards multiple directions firstly, as shown in region III, followed by the appearance of 1D periodic lattice fringes. The 1D type ordering atomic clusters comprised an array of planes in the same direction, typically along the low index or close packed direction, as shown in region IV. As nanocrystallization proceeded, the 1D periodicity evolved to a higher ordered structure through continuous atomic adjustment until nanocrystals form, as shown in **Fig. 8**. However, due to the short impacting period (~10^{-8} s [43]) and high cooling rates (10^9~10^{10} K s^{-1} [25]) in cold spray process, the nanocrystallization level was very limited, and consequently, only nano-scale crystals could be formed at localized regions. In fact, similar evolution was also observed during the nanocrystallization of Zr-based metallic glasses induced by high-density pulse-current treatment [41] and annealing [44,45]. Besides, the nanocrystallization process in amorphous Ni using molecular dynamics simulation method also showed the formation of ordered transition structure (1D and 2D structure) followed by 3D nanocrystals [41,45]. From the point view of thermodynamics, the energy barrier to form 3D nanocrystals directly is much higher than that to form low dimensional ordered transition structures. While from the kinetic aspect, more atomic rearrangement is required to form 3D nanocrystal, as compared to form transition quasi-ordered structures [45]. The evolution process of atomic structure from amorphous structure to 3D nanocrystals is probably universal. Thanks to the nature of cold spray (e.g., extremely rapid heating and cooling

rate, short impacting period, and high strain rate), the ordered atomic structures at different stages can be frozen and recorded, which offers us an opportunity to explore the nanocrystallization process of metallic glasses during cold spray process.

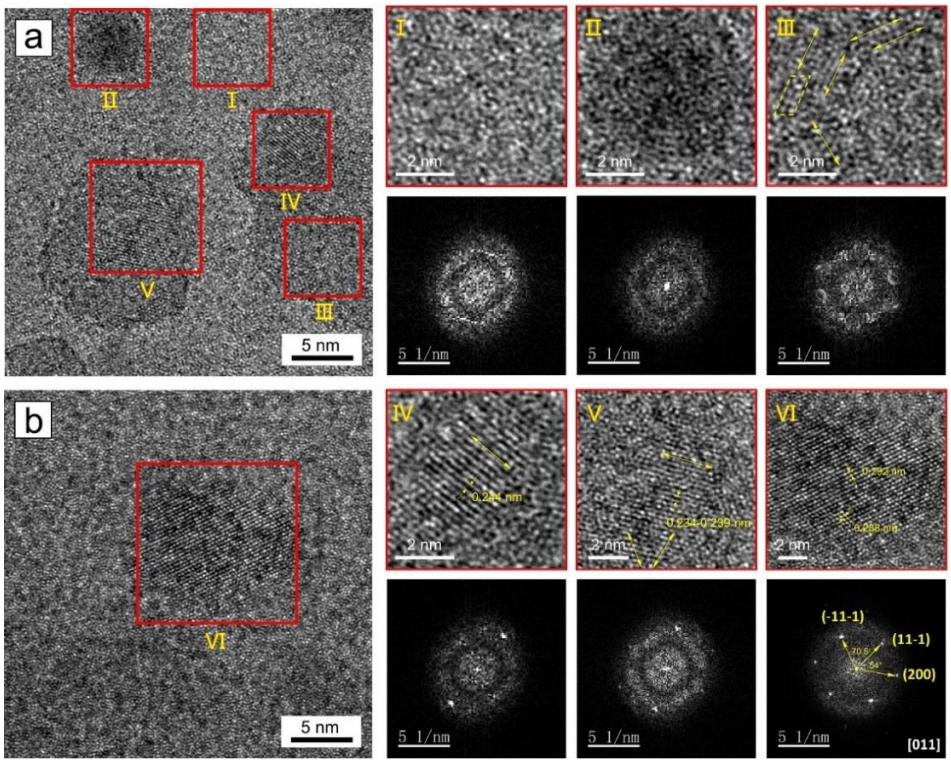

Figure 7. HRTEM images and corresponding FFT diffraction patterns of localized ordered clusters near interparticle interface: (a) localized ordered atomic configuration, (b) nanocrystal structure.

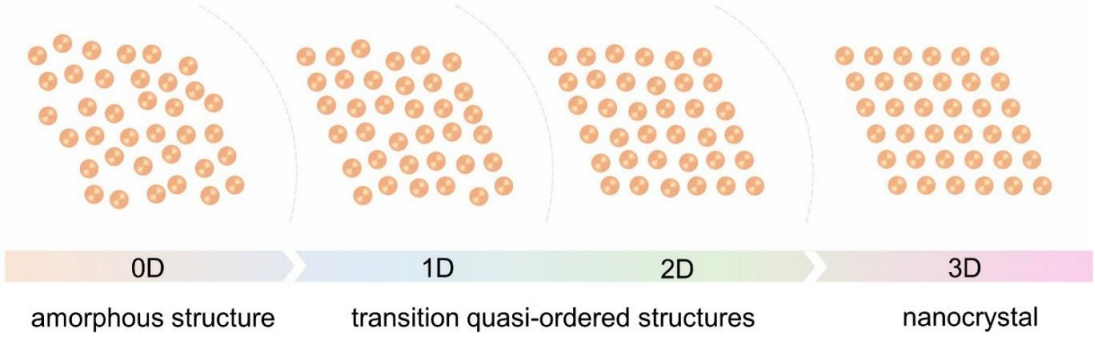

Figure 8. Evolution of nanocrystals from an amorphous state.

4 Conclusion

In this work, the bonding and nanocrystallization mechanisms of cold sprayed metallic glass particles were systematically investigated. Zr55 metallic glass powder were used as feedstock for cold spray deposition. Based on the results and discussion, a number of important conclusions that can significantly enrich our knowledge and understanding of cold sprayed BMG deposits were drawn and listed as follows:

1. For the first time, the exact bonding location of metallic glass particles was observed experimentally: interparticle bonding only occurred at the fringe area of interface, which can be attributed to the high-velocity impact induced localized metallurgical bonding.
2. A new mechanism that also contributed to the bonding of cold sprayed metallic glass particles was first found. Some metallic glass particles were subjected to partial melting inside the nozzle. The melted outer layer of a particle was forced to flow to periphery upon impact, and adhered with the substrate through an annular metallurgical bonding band.
3. Ordered atomic structures at different levels were randomly dispersed in the amorphous matrix near interparticle interface. The nanocrystallization at interfacial regions was mainly induced by mechanical factors (e.g., high strain and high strain rates) rather than adiabatic heating.
4. The different amorphous/nanocrystal structures in cold sprayed metallic glass particles can represent different evolution stages in the process of nanocrystallization. The formation of nanocrystals from amorphous state can

be divided into following stages: composition segregation, the formation of ordered 1D and 2D transition structure followed by the 3D nanocrystals.

Literature

[1] J.J. Kruzic, Bulk Metallic Glasses as Structural Materials: A Review, Adv. Eng. Mater. 18 (2016) 1308–1331. https://doi.org/10.1002/adem.201600066.

[2] M.M. Trexler, N.N. Thadhani, Mechanical properties of bulk metallic glasses, Prog. Mater. Sci. 55 (2010) 759–839. https://doi.org/10.1016/j.pmatsci.2010.04.002.

[3] H.Z. Wang, Y.H. Cheng, J.Y. Yang, Q.Q. Wang, Microstructure and properties of laser clad Fe-based amorphous alloy coatings containing Nb powder, J. Non. Cryst. Solids. 550 (2020) 120351. https://doi.org/10.1016/j.jnoncrysol.2020.120351.

[4] X. Lin, Y. Zhang, G. Yang, X. Gao, Q. Hu, J. Yu, L. Wei, W. Huang, Microstructure and compressive/tensile characteristic of large size Zr-based bulk metallic glass prepared by laser solid forming, J. Mater. Sci. Technol. 35 (2019) 328–335. https://doi.org/10.1016/j.jmst.2018.10.033.

[5] D. Ouyang, N. Li, L. Liu, Structural heterogeneity in 3D printed Zr-based bulk metallic glass by selective laser melting, J. Alloys Compd. 740 (2018) 603–609. https://doi.org/10.1016/j.jallcom.2018.01.037.

[6] C. Zhang, W. Wang, Y.C. Li, Y.G. Yang, Y. Wu, L. Liu, 3D printing of Fe-based bulk metallic glasses and composites with large dimensions and enhanced toughness by thermal spraying, J. Mater. Chem. A. 6 (2018) 6800–6805. https://doi.org/10.1039/c8ta00405f.

[7] G. Wang, Z. Huang, P. Xiao, X. Zhu, Spraying of Fe-based amorphous coating with high corrosion resistance by HVAF, J. Manuf. Process. 22 (2016) 34–38. https://doi.org/10.1016/j.jmapro.2016.01.009.

[8] J. Kim, K. Kang, S. Yoon, S. Kumar, H. Na, C. Lee, Oxidation and crystallization mechanisms in plasma-sprayed Cu-based bulk metallic glass coatings, Acta Mater. 58 (2010) 952–962. https://doi.org/10.1016/j.actamat.2009.10.011.

[9] J. Lu, G. Ravichandran, W.L. Johnson, Deformation behavior of the Zr41.2Ti13.8Cu12.5Ni10Be22.5 bulk metallic glass over a wide range of strain-rates and temperatures, Acta Mater. 51 (2003) 3429–3443. https://doi.org/10.1016/S1359-6454(03)00164-2.

[10] S. Yoon, H.J. Kim, C. Lee, Deposition behavior of bulk amorphous NiTiZrSiSn according to the kinetic and thermal energy levels in the kinetic spraying process, Surf. Coatings Technol. 200 (2006) 6022–6029. https://doi.org/10.1016/j.surfcoat.2005.09.022.

[11] S. Yoon, C. Lee, H. Choi, H. Kim, J. Bae, Impacting behavior of bulk metallic glass powder at an abnormally high strain rate during kinetic spraying, Mater. Sci. Eng. A. 448–451 (2007) 911–915. https://doi.org/10.1016/j.msea.2006.02.433.

[12] S. Yoon, C. Lee, H. Choi, H. Jo, Kinetic spraying deposition behavior of bulk amorphous NiTiZrSiSn feedstock, Mater. Sci. Eng. A. 415 (2006) 45–52. https://doi.org/10.1016/j.msea.2005.08.132.

[13] A. List, F. Gärtner, T. Mori, M. Schulze, H. Assadi, S. Kuroda, T. Klassen, Cold Spraying of Amorphous Cu50Zr50 Alloys, J. Therm. Spray Technol. 24 (2014) 108–118. https://doi.org/10.1007/s11666-014-0187-x.

[14] J. Henao, A. Concustell, S. Dosta, G. Bolelli, I.G. Cano, L. Lusvarghi, J.M. Guilemany, Deposition mechanisms of metallic glass particles by Cold Gas Spraying, Acta Mater. 125 (2017) 327–339. https://doi.org/10.1016/j.actamat.2016.12.007.

[15] Q.P. Cao, J.F. Li, Y.H. Zhou, A. Horsewell, J.Z. Jiang, Effect of rolling deformation on the microstructure of bulk Cu60Zr20Ti20 metallic glass and its crystallization, Acta Mater. 54 (2006) 4373–4383. https://doi.org/10.1016/j.actamat.2006.05.030.

[16] S. Shukla, D.T. Wu, H. Ramanarayan, D. Srolovitz, R. V. Ramanujan, Nanocrystallization in driven amorphous materials, Acta Mater. 61 (2013) 3242–3248. https://doi.org/10.1016/j.actamat.2013.02.012.

[17] E. Pekarskaya, J.F. Löffler, W.L. Johnson, Microstructural studies of crystallization of a Zr-based bulk metallic glass, Acta Mater. 51 (2003) 4045–4057. https://doi.org/10.1016/S1359-6454(03)00225-8.

[18] T. Nagase, Y. Umakoshi, Electron irradiation induced crystallization of the amorphous phase in Zr-Cu based metallic glasses with various thermal stability, Mater. Trans. 45 (2004) 13–23. https://doi.org/10.2320/matertrans.45.13.

[19] S. Yoon, G. Bae, Y. Xiong, S. Kumar, K. Kang, J.J. Kim, C. Lee, Strain-enhanced nanocrystallization of a CuNiTiZr bulk metallic glass coating by a kinetic spraying process, Acta Mater. 57 (2009) 6191–6199. https://doi.org/10.1016/j.actamat.2009.08.045.

[20] N. Fan, J. Cizek, C. Huang, X. Xie, Z. Chlup, R. Jenkins, R. Lupoi, S. Yin, A new strategy for strengthening additively manufactured cold spray deposits through in-process densification, Addit. Manuf. 36 (2020) 101626. https://doi.org/10.1016/j.addma.2020.101626.

[21] D. Ouyang, Q. Zheng, L. Wang, H. Wang, C. Yang, P. Zhang, N. Li, The brittleness of post-treatment of 3D printed Zr-based metallic glasses in supercooled liquid state, Mater. Sci. Eng. A. 782 (2020) 139259. https://doi.org/10.1016/j.msea.2020.139259.

[22] O. Haruyama, Y. Nakayama, R. Wada, H. Tokunaga, J. Okada, T. Ishikawa, Y. Yokoyama, Volume and enthalpy relaxation in Zr55Cu30Ni5Al10 bulk metallic glass, Acta Mater. 58 (2010) 1829–1836. https://doi.org/10.1016/j.actamat.2009.11.025.

[23] J.J. Lewandowski, A.L. Greer, Temperature rise at shear bands in metallic glasses, Nat. Mater. 5 (2006) 15–18. https://doi.org/10.1038/nmat1536.
[24] Y. Yokoyama, A. Inoue, Reply to Comments by Tsuyoshi Kajitani on Our Paper Titled 'Production of Zr55Cu30Ni5Al10 Glassy Alloy Rod of 30 mm in Diameter by a Cap-Cast Technique (by Y. Yokoyama, et al., Mater. Trans. 48 (2007) 3190–3192),' Mater. Trans. 50 (2009) 2504–2506. https://doi.org/https://doi.org/10.2320/matertrans.M2009258.
[25] T. Schmidt, F. Gärtner, H. Assadi, H. Kreye, Development of a generalized parameter window for cold spray deposition, Acta Mater. 54 (2006) 729–742. https://doi.org/10.1016/j.actamat.2005.10.005.
[26] B. Zheng, Y. Lin, Y. Zhou, E.J. Lavernia, Gas atomization of amorphous aluminum: Part I. thermal behavior calculations, Metall. Mater. Trans. B Process Metall. Mater. Process. Sci. 40 (2009) 768–778. https://doi.org/10.1007/s11663-009-9276-5.
[27] M. Zhang, Z. Zhang, Numerical simulation study on cooling of metal droplet in atomizing gas, Mater. Today Commun. 25 (2020) 101423. https://doi.org/10.1016/j.mtcomm.2020.101423.
[28] Z. Kovács, P. Henits, A.P. Zhilyaev, Á. Révész, Deformation induced primary crystallization in a thermally non-primary crystallizing amorphous Al85Ce8Ni5Co2 alloy, Scr. Mater. 54 (2006) 1733–1737. https://doi.org/10.1016/j.scriptamat.2006.02.004.
[29] J.J. Kim, Y. Choi, S. Suresh, A.S. Argon, Nanocrystallization during nanoindentation of a bulk amorphous metal alloy at room temperature, Science (80-.). 295 (2002) 654–657. https://doi.org/10.1126/science.1067453.
[30] S.H. Joo, D.H. Pi, A.D.H. Setyawan, H. Kato, M. Janecek, Y.C. Kim, S. Lee, H.S. Kim, Work-Hardening Induced Tensile Ductility of Bulk Metallic Glasses via High-Pressure Torsion, Sci. Rep. 5 (2015) 1–9. https://doi.org/10.1038/srep09660.
[31] G.J. Fan, M.X. Quan, Z.Q. Hu, W. Löser, J. Eckert, Deformation-induced microstructural changes in Fe 40 Ni 40 P 14 B 6 metallic glass, J. Mater. Res. 14 (1999) 3765–3774. https://doi.org/10.1557/JMR.1999.0510.
[32] S.W. Lee, M.Y. Huh, S.W. Chae, J.C. Lee, Mechanism of the deformation-induced nanocrystallization in a Cu-based bulk amorphous alloy under uniaxial compression, Scr. Mater. 54 (2006) 1439–1444. https://doi.org/10.1016/j.scriptamat.2006.01.002.
[33] Y.X. Zhuang, J.Z. Jiang, T.J. Zhou, H. Rasmussen, L. Gerward, M. Mezouar, W. Crichton, A. Inoue, Pressure effects on Al89La6Ni5 amorphous alloy crystallization, Appl. Phys. Lett. 77 (2000) 4133–4135. https://doi.org/10.1063/1.1332409.
[34] S.W. Lee, M.Y. Huh, E. Fleury, J.C. Lee, Crystallization-induced plasticity of Cu-Zr containing bulk amorphous alloys, Acta Mater. 54 (2006) 349–355. https://doi.org/10.1016/j.actamat.2005.09.007.
[35] W.H. Jiang, M. Atzmon, Mechanically-assisted nanocrystallization and defects in amorphous alloys: A high-resolution transmission electron microscopy study, Scr. Mater. 54 (2006) 333–336. https://doi.org/10.1016/j.scriptamat.2005.09.052.
[36] S. Yoon, Y. Xiong, K. Kang, G. Bae, C. Lee, Phase separation in kinetic sprayed bulk metallic glasses, J. Phys. D. Appl. Phys. 42 (2009) 182007. https://doi.org/10.1088/0022-3727/42/18/182007.
[37] Q.P. Cao, J.F. Li, Y.H. Zhou, A. Horsewell, J.Z. Jiang, Free-volume evolution and its temperature dependence during rolling of Cu60Zr20Ti20 bulk metallic glass, Appl. Phys. Lett. 87 (2005) 101901. https://doi.org/10.1063/1.2037858.
[38] B.J. Park, H.J. Chang, D.H. Kim, W.T. Kim, In situ formation of two amorphous phases by liquid phase separation in Y-Ti-Al-Co alloy, Appl. Phys. Lett. 85 (2004) 6353–6355. https://doi.org/10.1063/1.1842360.
[39] A. Takeuchi, A. Inoue, Classification of Bulk Metallic Glasses by Atomic Size Difference, Heat of Mixing and Period of Constituent Elements and Its Application to Characterization of the Main Alloying Element, Mater. Trans. 46 (2005) 2817–2829. https://doi.org/10.2320/matertrans.46.2817.
[40] G.L. Chen, X.J. Liu, X.D. Hui, H.Y. Hou, K.F. Yao, C.T. Liu, J. Wadsworth, Molecular dynamic simulations and atomic structures of amorphous materials, Appl. Phys. Lett. 88 (2006) 20–23. https://doi.org/10.1063/1.2198015.
[41] X.J. Liu, G.L. Chen, H.Y. Hou, X. Hui, K.F. Yao, Z.P. Lu, C.T. Liu, Atomistic mechanism for nanocrystallization of metallic glasses, Acta Mater. 56 (2008) 2760–2769. https://doi.org/10.1016/j.actamat.2008.02.019.
[42] S.-T. Yau, P.G. Vekilov, Quasi-planar nucleus structure in apoferritin crystallization, Nature. 406 (2000) 494–497. https://doi.org/10.1038/35020035.
[43] J. Wu, H. Fang, H.J. Kim, C. Lee, High speed impact behaviors of Al alloy particle onto mild steel substrate during kinetic deposition, Mater. Sci. Eng. A. 417 (2006) 114–119. https://doi.org/10.1016/j.msea.2005.11.011.
[44] X.J. Liu, X.D. Hui, G.L. Chen, M.H. Sun, In situ synchrotron SAXS study of nanocrystallization in Zr65Ni25Ti10 metallic glass, Intermetallics. 16 (2008) 10–15. https://doi.org/10.1016/j.intermet.2007.06.014.
[45] X.J. Liu, G.L. Chen, F. Li, X.D. Hui, Z.P. Lu, F. Ye, C.T. Liu, Evolution of atomic ordering in metallic glasses, Intermetallics. 18 (2010) 2333–2337. https://doi.org/10.1016/j.intermet.2010.08.004.